Bio-Design and Manufacturing (2023) 6:121–135
https://doi.org/10.1007/s42242-022-00222-2

RESEARCH ARTICLE

Direct ink writing to fabricate porous acetabular cups from titanium alloy

Naima Valentin[1] · Weijian Hua[1] · Ashish K. Kasar[1] · Lily Raymond[1] · Pradeep L. Menezes[1] · Yifei Jin[1]

Received: 18 July 2022 / Accepted: 13 November 2022 / Published online: 28 December 2022

Abstract

Acetabular cups, which are among the most important implants in total hip arthroplasty, are usually made from titanium alloys with high porosity and adequate mechanical properties. The current three-dimensional (3D) printing approaches to fabricate customized acetabular cups have some inherent disadvantages such as high cost and energy consumption, residual thermal stress, and relatively low efficiency. Thus, in this work, a direct ink writing method was developed to print a cup structure at room temperature, followed by multi-step heat treatment to form microscale porous structure within the acetabular cup. Our method is facilitated by the development of a self-supporting titanium-6 aluminum-4 vanadium (Ti64) ink that is composed of Ti64 particles, bentonite yield-stress additive, ultraviolet curable polymer, and photo-initiator. The effects of Ti64 and bentonite concentrations on the rheological properties and printability of inks were systematically investigated. Moreover, the printing conditions, geometrical limitations, and maximum curing depth were explored. Finally, some complex 3D structures, including lattices with different gap distances, honeycomb with a well-defined shape, and an acetabular cup with uniformly distributed micropores, were successfully printed/fabricated to validate the effectiveness of the proposed method.

Graphic abstract

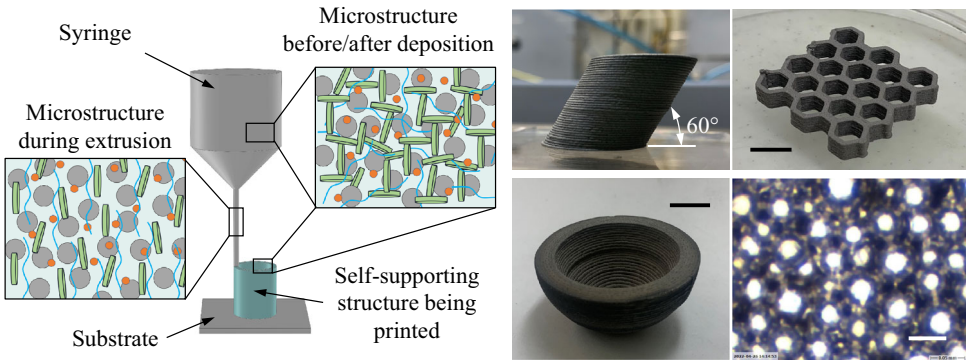

Keywords Acetabular cup · Direct ink writing · Titanium alloy · Bentonite · Heat treatment

Introduction

Total hip arthroplasty is a kind of surgery that replaces worn-out or damaged hip joints using a prosthetic implant, which can effectively relieve arthritis pain and/or heal certain hip fractures. Each year, over 1.4 million total hip arthroplasty procedures are performed worldwide [1–3]. In the USA alone, this number is expected to grow significantly to around

✉ Yifei Jin
yifeij@unr.edu

[1] Mechanical Engineering Department, University of Nevada, Reno, Reno, NV 89557, USA

2 million by 2040 [4]. Acetabular cups are some of the widely used implants in total hip arthroplasty, which are generally prepared from titanium alloys with high porosity and suitable mechanical properties [1–3] to facilitate bone ingrowth and osseointegration after implantation [5, 6]. In particular, titanium-6 aluminum-4 vanadium (Ti64) has been commonly used as the principal material for fabricating acetabular cups due to its high strength, low density, and excellent biocompatibility with bone [7–9].

The conventional process to fabricate titanium acetabular cups usually begins with a dense block of solid titanium that is subsequently shaped through either computer numerical control (CNC) machining, powder metallurgy, forging, or casting [8]. CNC machining, while capable of manufacturing custom parts, wastes a significant amount of material, increasing the cost of the final product. In addition, it is difficult to create microscale porous structures within an acetabular cup through this subtractive manufacturing strategy. For powder metallurgy, forging, and casting, although it is feasible to reduce the material waste during fabrication, these methods all require extensive tooling such as molds before a part can be created, making it challenging to fabricate customized acetabular cups at a relatively low cost. The development of additive manufacturing technology, commonly known as three-dimensional (3D) printing [10], provides an alternative solution for this task. Because 3D objects are printed in a layer-by-layer fashion, it is relatively easy to control the intralayer architectures, enabling the creation of porous structures [5, 11]. Moreover, 3D printing is known for its ability to customize products on demand and reduce material waste significantly [12, 13]. As a result, it has become the mainstream strategy for manufacturing acetabular cups.

Among the various 3D printing approaches, the most commonly used ones to make commercially available acetabular cups are selective laser sintering (SLS) [14, 15] and electron beam melting (EBM) [16–19], two sub-techniques of powder bed fusion [20]. They utilize a high-energy laser or electron to provide high energy to the surface of a powder bed in the form of a beam spot. Metal particles under the beam spot have transient temperatures exceeding 2000 °C, leading to their molten state. When the beam spot moves away, the temperature locally drops at an extremely high cooling rate of ~104 °C/s [21], resulting in the sintering of metal particles. Thus, by moving the beam spot based on designed trajectories, an acetabular cup can be printed in a pixel-by-pixel manner. Nevertheless, these techniques have several limitations: (1) The use of laser beam or electron beam increases the cost and energy consumption of acetabular cup fabrication; (2) The high printing temperature and rapid cooling process lead to the generation of internal stress, weakening the mechanical properties of printed acetabular cups; (3) The microscale beam spot (0.5–1.5 μm for SLS and 2–3 μm for EBM) facilitates the printing of micropores with high resolution but inhibits the fabrication of macroscale cups with high efficiency. As a result, it is still important to investigate new printing techniques to fabricate acetabular cups at lower temperatures, reduced cost, and higher efficiency.

Direct ink writing, a material extrusion 3D printing strategy, is becoming one of the most commonly used additive manufacturing techniques based on its low cost, high printing efficiency, wide range of printable materials, and easy implementation [22, 23]. In direct ink writing, liquid build material is extruded through a dispensing nozzle to form continuous cylindrical filaments, which are rapidly solidified/cured/crosslinked and then stacked into 3D structures layer by layer. In recent years, this method has also been adopted in metal 3D printing applications. For example, Elsayed et al. [24] developed a Ti64-based ink composed of polyvinyl alcohol and polyethylene glycol as the solvent and Ti64 powders as the metal phase, and successfully printed highly porous 3D lattices. Xu et al. [25] demonstrated the printability of the ink with titanium dioxide powders in an aqueous solution of Pluronic F127 by creating 3D structures with hierarchically macro- and microscale porosity. Pack et al. [26] used red seaweed-derived polysaccharide, serving as both binder and viscosifier, along with stainless steel or nickel powders and dispersants to prepare the self-supporting ink. They used direct ink writing to print the complex metallic architectures such as honeycomb and lattice. Peng et al. [27] mixed pre-alloyed high-entropy powders (i.e., CoCrFeNiMn) with organic solvent as the ink to print 3D structures in air. In the aforementioned studies, metallic powders need to be mixed with solvents to prepare suspensions/pastes as metal-laden inks. After being extruded, the solvents rapidly evaporate to cause the solidification of a printed layer, which will thus have the mechanical stiffness to hold the subsequent deposited layers. However, this solvent evaporation-induced solidification mechanism cannot provide strong adhesion between adjacent layers, leading to poor interlayer bonding. Therefore, only architectures with simple geometries such as lattices and honeycombs have been printed using this approach; it is challenging to fabricate complex acetabular cups with large dimensions and overhangs from the solvent-based metal-laden inks. In addition, the pore size in these structures is mainly determined by the size of each printed lattice in the order of millimeters [24–26], and creating microscale pores (from tens to hundreds of microns) is still a technical challenge. As a result, it is of great significance to explore new direct ink writing strategies that are able to achieve the fabrication of macroscale acetabular cups, as well as facilitate the formation of microscale porous structures within the printed cups.

In this study, a self-supporting matrix ink composed of microscale bentonite additive and poly(ethylene glycol)

diacrylate (PEGDA) was investigated by mixing Ti64 powders in to prepare Ti64-based ink (hereinafter referred to as Ti64 ink). The bentonite additive can inherently form a microstructure within the Ti64 ink, which not only makes the ink self-supporting for direct ink writing, but also stably traps Ti64 powders in situ, effectively preventing aggregation-induced nozzle clogging. The introduction of PEGDA enables the ink to be ultraviolet (UV) curable, thus providing strong, long-lasting structural support to the printed architecture. Therefore, acetabular cups from the Ti64 ink can be easily printed via direct ink writing at room temperature because of the dual supporting mechanisms offered by bentonite and crosslinked PEGDA. After printing, a multi-step heat treatment process was used to burn out bentonite and PEGDA as well as sinter Ti64 powders together to form micropores within the Ti64 acetabular cups. In this way, this study offers a highly efficient, relatively energy-sustainable, and cost-effective manufacturing approach for fabricating porous 3D titanium structures with complex geometries, that can be valuable not only in biomedical applications, but also in other major fields such as the aerospace and automotive industries.

Materials and methods

Ti64 ink preparation

Firstly, the self-supporting matrix ink without Ti64 powder was prepared. Stock PEGDA (M_n 700, Sigma-Aldrich, St. Louis, MO, USA) was diluted by deionized (DI) water to prepare a solution with a concentration of 30% (v/v). Then, photo-initiator (2-hydroxy-4'-(2-hydroxyethoxy)-2-methylpropiophenone, Sigma-Aldrich, St. Louis, MO, USA) was added to the diluted PEGDA solution at the concentration of 2% (w/v) and manually mixed at room temperature until the photo-initiator powder was completely dissolved. Subsequently, an appropriate amount of bentonite powder (Bentonite® clay, BYK Additives Inc., Gonzales, TX, USA) was dispersed into the solution and mixed manually via a glass rod for a minimum of 10 min at room temperature. The prepared matrix ink was stored in the dark in a sealed container to prevent degradation and evaporation, and aged for one day before mixing with Ti64 powder. To prepare the Ti64 ink, an appropriate amount of Ti64 powder (Ti–6Al–4 V grade 5, AP&C, Boisbriand, Canada) with the average size of 45–106 μm was dispersed into the self-supporting matrix ink and mixed manually using a glass rod until the Ti64 powder was uniformly distributed. Then, the prepared Ti64 ink was loaded into a syringe barrel for printing.

For rheological property characterization, two baths of Ti64 inks were prepared: one had 50% (v/v) Ti64 powder for mixing with the self-supporting matrix inks with bentonite concentrations of 3%, 4%, and 5% (w/v); the other had 40%, 50%, and 60% (v/v) Ti64 powder for mixing with the matrix ink with 4% (w/v) bentonite. In addition, Ti64 inks with 40% (v/v) Ti64 and 4% (w/v) bentonite, 50% (v/v) Ti64 and 4% (w/v) bentonite, 50% (v/v) Ti64 and 3% (w/v) bentonite, as well as 50% (v/v) Ti64 and 5% (w/v) bentonite, were prepared for the filament deflection test. Meanwhile, Ti64 inks with 40% (v/v) Ti64 and 4% (w/v) bentonite, 50% (v/v) Ti64 and 3% (w/v) bentonite, 50% (v/v) Ti64 and 4% (w/v) bentonite, 50% (v/v) Ti64 and 5% (w/v) bentonite, as well as 60% (v/v) Ti64 and 4% (w/v) bentonite, were prepared for vertical tube printing. The Ti64 ink with 50% (v/v) Ti64 and 4% (w/v) bentonite was selected for evaluating the operating conditions and the printing of complex 3D structures.

Characterization of rheological properties

The rheological properties of the Ti64 inks with different concentrations were characterized using a rheometer (MCR 92, Anton Paar GmbH, Graz, Austria) equipped with a parallel-plate measuring tool (50 mm in diameter and 1 mm gap distance). The steady shear rate sweeps were performed to measure the yield stress and viscosity of each Ti64 ink by varying the shear rate from 0.01 to 100 s^{-1}. All tests were conducted at room temperature.

Printing system and protocol

A material extrusion 3D printer (3D Bioplotter, EnvisionTEC GmbH, Gladbeck, Germany) was used for all printing experiments at room temperature. To investigate the effects of dispensing pressure, the Ti64 ink was first extruded through a 20-gauge dispensing nozzle (EFD Nordson, Vilters, Switzerland) to form continuous filaments on a glass slide (VistaVisionTM, VWR International, PA, USA). The path speed and standoff distance (the distance between the nozzle tip and substrate) were set at 7 mm/s and 0.75 mm, respectively, while the dispensing pressure was increased from 0.1 to 0.5 bar (1 bar=100 kPa) with an interval of 0.1 bar. Then, the same dispensing nozzle (20-gauge) was used for filament printing at different path speeds (5, 6, 7, 8, and 9 mm/s), which were selected based on the preliminary experiments. The dispensing pressure was controlled at 0.3 bar and the standoff distance was set at 0.75 mm. Finally, different standoff distances were selected, including 0.25, 0.50, 0.75, 1.00, and 1.25 mm, to print filaments from the Ti64 ink. The dispensing pressure, nozzle, and path speed were set at 0.3 bar, 20-gauge, and 7 mm/s, respectively.

For inclined tube printing, the key printing conditions were set as follows: 20-gauge dispensing nozzle, dispensing pressure of 0.3 bar, path speed of 7 mm/s, and standoff distance of 0.75 mm. The step distance along the vertical direction was controlled at 0.7 mm. Thus, the tubes with the

designed diameter of 20 mm and inclined angles of 30°, 45°, and 60° were printed on the substrate. In addition, the 20-gauge dispensing nozzle was used to print the honeycomb in an overall size of 20 mm × 20 mm × 8 mm. The dispensing pressure was 0.3 bar, the path speed was 7 mm/s, the standoff distance was 0.75 mm, and the step distance was 0.7 mm. The same printing conditions were used for the direct ink writing of five-layered lattices with a length of 20 mm, width of 20 mm, and different gap distances of 3, 4, and 5 mm.

Digital 3D models of the fabricated 3D structures were designed using SolidWorks 2022 (Dassault Systemes SolidWorks Corp., Waltham, MA, USA). The 3D models were loaded into the 3D printer's software (Perfactory RP, EnvisionTEC GmbH, Gladbeck, Germany) for slicing, and then printed by the 3D printer.

Print characterization

In order to study the filament deflection, a supporting tool was designed in SolidWorks 2022 (Dassault Systemes SolidWorks Corp., Waltham, MA, USA) with seven gap distances (including 0.5, 1.0, 2.0, 4.0, 6.0, 8.0, and 10.0 mm), and then fabricated using a fused deposition modeling (FDM) 3D printer (Ender-3 Pro, Shenzhen Creality 3D Technology Co. Ltd., Shenzhen, China). The filaments from the Ti64 inks with different concentrations were extruded through the 20-gauge dispensing nozzle and deposited on the supporting tool. The dispensing pressure was 0.3 bar, the path speed was 7 mm/s, and the standoff distance was 0.75 mm. The filament deflection in each gap was imaged by a digital camera (DC-FZ80, Panasonic, Osaka, Japan), and the images were further analyzed by ImageJ software (https://imagej.nih.gov/ij/).

In order to investigate the self-supporting capability, the 20-gauge dispensing nozzle was used to print vertical tubes with the designed dimensions (including outer diameter (D_o) of 20.0 mm, wall thickness of 0.8 mm, and height (H_o) of 20.0 mm) from the Ti64 inks with different concentrations. The dispensing pressure was 0.3 bar, the path speed was 7 mm/s, the standoff distance was 0.75 mm, and the step distance was 0.7 mm. The digital camera was used to take a photograph of each printed tube and the key dimensions, including the actual outer diameter (D_p) and height (H_p), which were then measured by ImageJ. The relative errors of diameter and height were calculated by $r_D = \frac{D_p - D_o}{D_o} \times 100\%$ and $r_H = \frac{H_o - H_p}{H_o} \times 100\%$, respectively.

In order to study the effects of standoff distance on shape fidelity, the Ti64 ink with 50% (v/v) Ti64 and 4% (w/v) bentonite was printed on the substrate based on a pre-defined rectangular trajectory (20 mm × 20 mm). The image of each printed pattern was taken by a high-precision measurement system (Vertex 261 Micro-Vu, Windsor, CA, USA). The distance between the designed path and the printed pattern at one corner was defined as corner distance, which was used to quantify the shape fidelity.

Curing depth under UV radiation

The curing depth was measured to determine the maximum penetration and curing of the proposed ink material. First, the Ti64 ink with 50% (v/v) Ti64 and 4% (w/v) bentonite was filled into a cylindrical polydimethylsiloxane (PDMS) mold with a diameter of 12 mm and depth of 5 mm. Then, a UV curing system (OmniCure Series 2000, wavelength: 320–500 nm, Lumen Dynamics, Mississauga, Canada) was placed above the mold to cure the Ti64 ink for different time periods (from 5 to 75 min, with an interval of 5 min). The distance between the UV light and the mold top surface was controlled at 10 cm. After curing for each time period, the Ti64 sample was released from the mold. The thickness of the solidified Ti64 sample was measured and taken as the curing depth.

Acetabular cup fabrication

A cup structure with a designed diameter of 40 mm, height of 20 mm, and wall thickness of 5 mm was printed using the Ti64 ink with 50% (v/v) Ti64 and 4% (w/v) bentonite. The printing conditions were summarized as follows: 20-gauge nozzle, dispensing pressure of 0.3 bar, path speed of 7 mm/s, standoff distance of 0.75 mm, and step distance of 0.7 mm. To avoid large overhang-induced structural collapse, the cup was printed by two printing trajectories. For the bottom layers (height below 18 mm), the conventional concentric trajectory was used, while for the top layers (height from 18 to 20 mm), the parallel trajectory was applied to stack straight filaments in each layer. After printing, the cup structure was exposed to UV radiation for 60 min to cause the photo-crosslinking of the PEGDA phase. Thus, the green part with sufficient mechanical stiffness was obtained.

Next, multi-step heat treatment was performed to the cup structure using a single zone vacuum tube furnace (1700 °C 1-zone, Across International, NJ, USA) equipped with an alumina tube (60 mm × 1000 mm in size, CT-60-100, Across International, NJ, USA). During the process, the furnace pressure was controlled at a vacuum pressure of −0.9 bar. First, the furnace temperature was increased to 500 °C at a heating rate of 10 °C/min, and this temperature was kept for 2 h to burn out the PEGDA and photo-initiator. Then, the temperature was increased to 800 °C at a heating rate of 10 °C/min and maintained for 2 h to decompose the bentonite additive. To sinter the Ti64 particles together, the furnace temperature was raised to 1250 °C at a heating rate of 10 °C/min and then maintained at this value for 2 h. Finally, the furnace was cooled down to room temperature at a cooling rate of 10 °C/min.

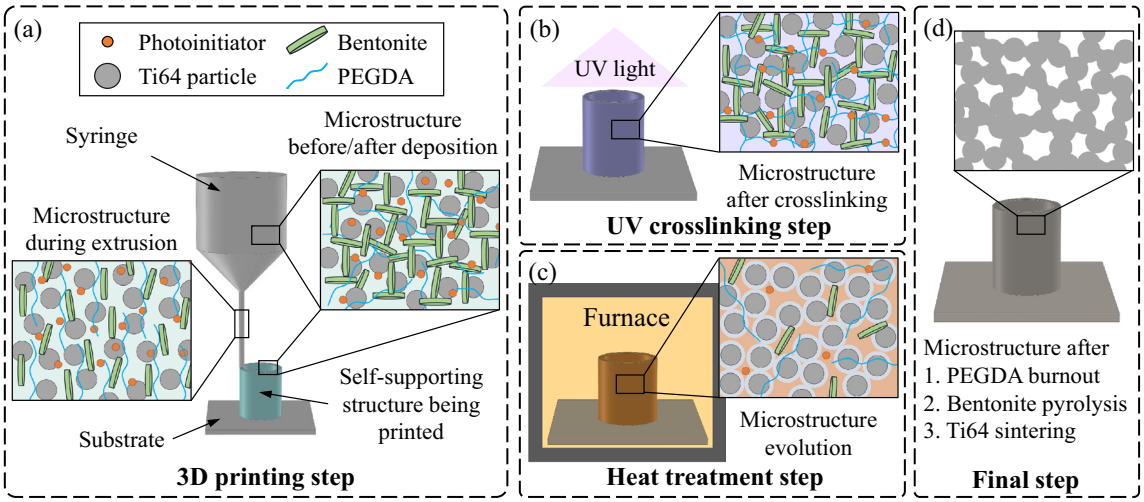

Fig. 1 Schematic of acetabular cup fabrication approach: **a** cup structure printing at room temperature via direct ink writing; **b** cup structure crosslinking under ultraviolet (UV) radiation; **c** heat treatment to form porous microstructure; **d** acetabular cup with uniformly distributed pores of the required sizes

After heat treatment, the acetabular cup was released from the furnace, and the surface morphology was imaged by the high-precision measurement system. Based on the obtained images, the pore dimensions and size distribution were further analyzed using ImageJ. In addition, the key dimensions of the acetabular cup (height, wall thickness, and outer diameter) before and after heat treatment were measured and compared to the designed dimensions.

Statistical analysis

All quantitative values in the text and figures were reported as means ± standard deviation (SD) with n (n=3) samples per group. Statistical analysis was performed using analysis of variance (ANOVA), and p values of less than 0.05 were considered as indicative of statistical significance.

Results and discussion

Mechanism of acetabular cup fabrication approach

The proposed acetabular cup fabrication approach consists of three main steps: (1) cup structure printing, (2) cup structure crosslinking, and (3) heat treatment, as shown in Fig. 1. In the first step, Ti64 ink is printed into a cup structure via direct ink writing at room temperature. The core of this step is the design of suitable Ti64-laden inks. Herein, Ti64 particles are mixed with a self-supporting matrix ink that is composed of bentonite particles and PEGDA. Bentonite is a member of the smectite mineral family with a broad range of particle sizes ranging from tenths to hundreds of microns. When dispersed in an aqueous-based solvent, each bentonite disk-shaped particle presents negative and positive charges on the surfaces and edge, respectively, leading to the formation of a rigid "house-of-cards" microstructure in the solvent, similar to that of nanoclay additive [28–30]. This inherent microstructure can stably trap Ti64 particles in situ to effectively prevent metal particle aggregation in a syringe (inset of Fig. 1a). During printing, Ti64 ink in a dispensing nozzle experiences shear stress that is higher than a threshold value, called yield stress [31], resulting in the disruption of the "house-of-cards" microstructure. Ti64 ink presents a shear-thinning behavior and can be easily extruded through the nozzle (inset of Fig. 1a) to form filaments. After extrusion, the microstructure of bentonite recovers, which enables the filaments to possess a high self-supporting capability, firmly holding the subsequently extruded filaments/layers. Thus, the cup structure can maintain the as-deposited shape before undergoing solidification. In the second step, because of the existence of PEGDA, the cup structure is photo-crosslinkable under UV radiation. PEGDA polymer chains are bonded by photo-initiators to form a stiffer and more stable 3D-networked structure [32], which provides the cup structure with sufficient mechanical properties for subsequent operations, as shown in Fig. 1b. In the last step, a multi-step heat treatment is performed, which aims to remove all unnecessary components (PEGDA, photo-initiator, and bentonite), generate microscale pores within the cup, and enhance the mechanical properties of the cup structure by sintering Ti64 particles together (Fig. 1c). In this work, the bentonite particle size is selected to be around 30–50 μm, which is close to the required pore size of acetabular cups. After pyrolyzing, microscale pores are able to form in the places originally

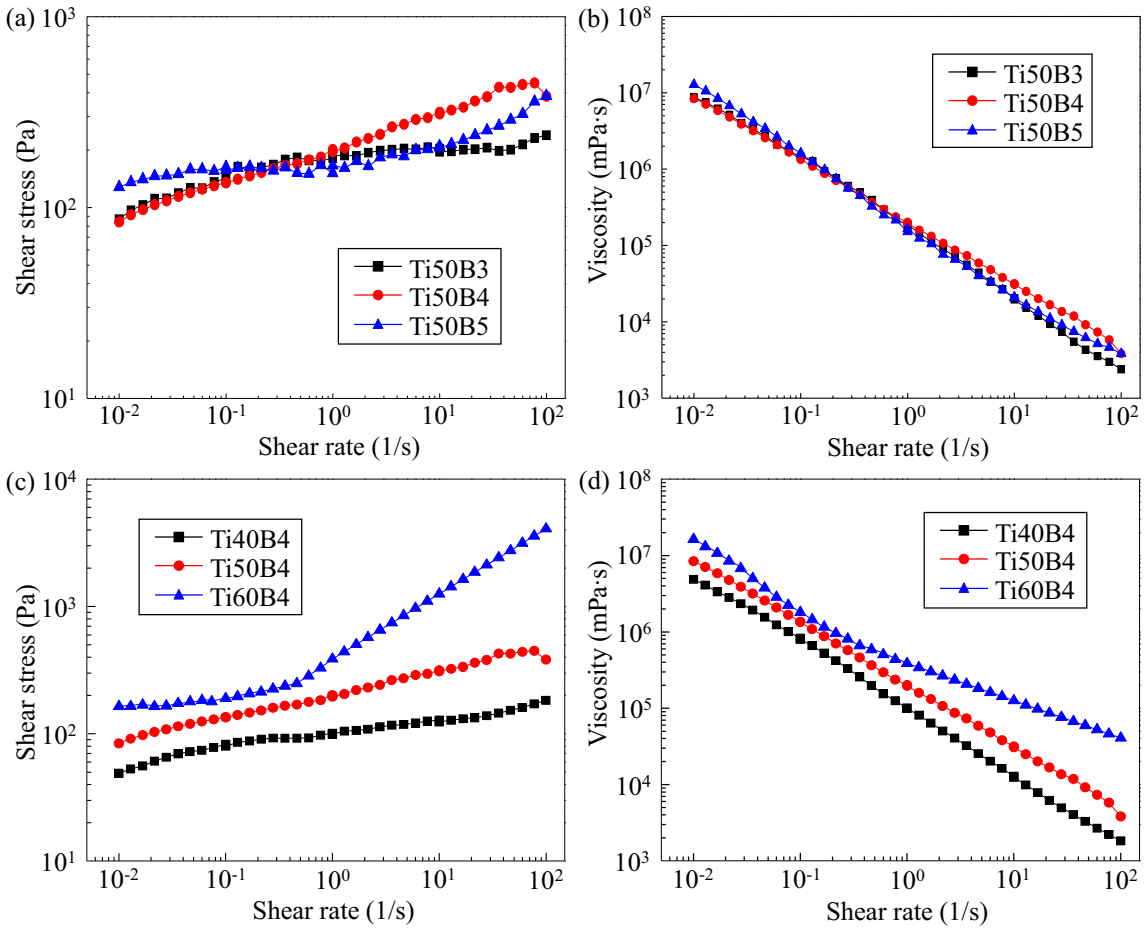

Fig. 2 Shear stress (**a**) and viscosity (**b**) as a function of shear rate of the Ti64 inks with 50% (v/v) Ti64 and 3%, 4%, and 5% (w/v) bentonite (marked as Ti50B3, Ti50B4, and Ti50B5, respectively). Shear stress (**c**) and viscosity (**d**) as a function of shear rate of the Ti64 inks with 40%, 50%, and 60% (v/v) Ti64 and 4% (w/v) bentonite (marked as Ti40B4, Ti50B4, and Ti60B4, respectively)

occupied by bentonite particles. When completing the heat treatment, the cup structure with micropores can be collected from the furnace and used as an acetabular cup after certain post-treatments (Fig. 1d).

Effects of Ti64 and bentonite on the rheological properties

Since Ti64 and bentonite are the two most important components in the Ti64 ink, their effects on the rheological properties were characterized. First, the shear stress–shear rate curves and the viscosity–shear rate curves of the Ti64 inks with 50% (v/v) Ti64 and 3%, 4%, and 5% (w/v) bentonite were measured and are illustrated in Figs. 2a and 2b, respectively. From Fig. 2a, it is found that when the bentonite concentration was changed, the yield stress did not show pronounced variation. Based on the Herschel–Bulkley model, that is, $\tau = \tau_0 + k\dot{\gamma}^n$, where τ denotes the shear stress, τ_0 denotes the yield stress, k denotes the consistency index, $\dot{\gamma}$ denotes the shear rate, and n is the flow index, the yield stresses of these inks were calculated as 131.3, 130.0, and 134.6 Pa, respectively (Table 1). From Fig. 2b, it can be seen that the viscosity of the inks decreased with the increasing shear rate, which indicated that these Ti64 inks presented shear-thinning behavior during extrusion. This is because when the shear stress exceeds the yield stress, the "house-of-cards" microstructure is disrupted. Disk-shaped bentonite

Table 1 Yield stress of the Ti64 inks with different formulas

Ti64 ink	Yield stress (Pa)	Viscosity (mPa·s)
Ti40B4	118.0	1.79×10^7
Ti50B3	131.3	3.24×10^7
Ti50B4	130.0	4.03×10^7
Ti50B5	134.6	5.84×10^7
Ti60B4	180.0	3.65×10^8

particles and PEGDA polymer chains are oriented under shear stress, leading to the decrease in viscosity [33]. By fitting the viscosity (η)–shear rate data into the Carreau-like model, that is, $\eta(\dot{\gamma}) = \frac{\eta_0}{1+(k\dot{\gamma})^n}$ [34, 35], the zero-shear-rate viscosity (η_0) of each Ti64 ink can be calculated, as shown in Table 1. Because the Ti64 concentration is much higher than the bentonite concentration, the large volume of Ti64 particles dominates the rheological properties of the inks. Thus, the change in bentonite concentration from 3% to 5% (w/v) cannot significantly affect the yield stress and the viscosity.

The shear stress and viscosity of the Ti64 inks with the same bentonite concentration (4% (w/v)) but different Ti64 concentrations are illustrated in Figs. 2c and 2d, respectively. As shown in Fig. 2c, the yield stress of the Ti64 inks increased when the Ti64 concentration was increased from 40% to 60% (v/v). Based on the Herschel–Bulkley model, the yield-stress values were calculated as 118.0, 130.0, and 180.0 Pa, respectively. In addition, the viscosity of the ink with 60% (v/v) Ti64 was the highest among the three inks. All inks showed shear-thinning behavior under shear stress, as illustrated in Fig. 2d, and the zero-shear-rate viscosities were calculated, as shown in Table 1. Thus, it was concluded that the rheological properties of the Ti64 ink are more sensitive to the change in Ti64 concentration.

Effects of Ti64 and bentonite on printability

Ti64 and bentonite further affected the printability of Ti64 inks. In this work, printability was quantified by two significant features: extrudability and formability [36]. The former is the capability of extruding continuous filaments through a dispensing nozzle, which is characterized by the shear-thinning behavior and zero-shear-rate viscosity of the ink material. Although all Ti64 inks presented shear-thinning behaviors (Figs. 2b and 2d), the zero-shear-rate viscosity of the ink with 60% (v/v) Ti64 and 4% (w/v) bentonite (3.65×10^8 mPa·s) was much higher than that of the other inks (1.79×10^7–5.84×10^7 mPa·s) (Table 1). Thus, it was difficult to extrude this Ti64 ink to form continuous filaments, as illustrated in Fig. 3a, which indicated that higher Ti64 concentration may weaken the extrudability of ink materials. It was noted that Ti64 particle size can also affect the extrudability of the inks: when the particle size is close to a nozzle inner diameter, nozzle clogging may occur, which inhibits filament extrusion; in contrast, when the particle size is relatively small, it is easier to uniformly disperse Ti64 particles in the matrix ink and extrude through a dispensing nozzle with a tiny orifice, resulting in the formation of fine filaments and subsequently printed 3D structures with high resolution. Because the average size of Ti64 powder in this work was 45–106 μm, a 20-gauge nozzle (inner diameter of ~600 μm) was selected to eliminate the effects of particle size on extrudability.

Formability is the capability of the ink material to mold self-supporting structures before crosslinking, which is determined by both yield stress and zero-shear-rate viscosity. In particular, yield stress indicates the threshold force/stress to induce the liquid–solid-like transition of the ink. After extrusion, the shear rate of ink is decreased to zero, and the zero-shear-rate viscosity is helpful to qualitatively assess the ability of the ink to maintain the shape. To explore the formability of different Ti64 inks, two structures (including vertical tube and simply supported filament beam) were selected. First, vertical tubes were printed on a substrate. The relative errors of diameter and height were measured as shown in Fig. 3a. It was found that, when the Ti64 concentration was relatively low (e.g., 40% (v/v)), the ink material possessed a low yield stress of 118.0 Pa and low zero-shear-rate viscosity of 1.79×10^7 mPa·s, presenting poor self-supporting capability, and the subsequent collapse of the printed tube during the printing process. When the Ti64 concentration was controlled at 50% (v/v), the yield stress of the ink materials was increased (130.0–134.6 Pa) and the zero-shear-rate viscosity fell in the range of 3.24×10^7–5.84×10^7 mPa·s, improving the formability and facilitating the printing of vertical tubes with relative errors below 10%. In addition, as seen from Fig. 3a, the increase in bentonite concentration further enhanced the formability: both the diameter relative error and the height relative error decreased when the bentonite concentration was increased from 3% to 5% (w/v). As a result, the printed tubes presented diameters and heights close to the designed values. Formability can be theoretically analyzed by calculating the maximum height of a vertical tube based on the ink density (ρ) and yield shear stress (τ_y=τ_0). When the vertical tube is printed in air, its bottom suffers the highest compression stress ($\sigma_M = \rho g H_v$, where σ_M denotes the highest compression stress, g denotes the gravitational acceleration, and H_v denotes the maximum height). The tube can stand in air without collapse as long as σ_M is lower than the yield normal stress (σ_y), which can be calculated by $\sigma_y = 3\tau_y/\sqrt{2}$ [28]. Thus, the maximum height of the Ti40B4 tube is 10.03 mm, while the heights of the Ti50B3, Ti50B4, and Ti50B5 tubes are 9.87, 9.75, and 10.08 mm, respectively, which are very close to each other. Because the designed height of the vertical tubes is 20.00 mm, which exceeds their maximum heights, all tubes are supposed to collapse. However, since the zero-shear-rate viscosities of the inks with 50% (v/v) Ti64 are approximately 1.8 to 3.2 times higher than the viscosity of the ink with 40% (v/v) Ti64 (Table 1), these tubes stably maintain their as-deposited shapes in air. Only the tube made from Ti40B4 collapses, as shown in the inset of Fig. 3a.

Next, the filament beams made from the Ti64 inks with different compositional concentrations were printed on the supporting tool with increasing gap distance, and their deflections were measured to characterize their formability, as

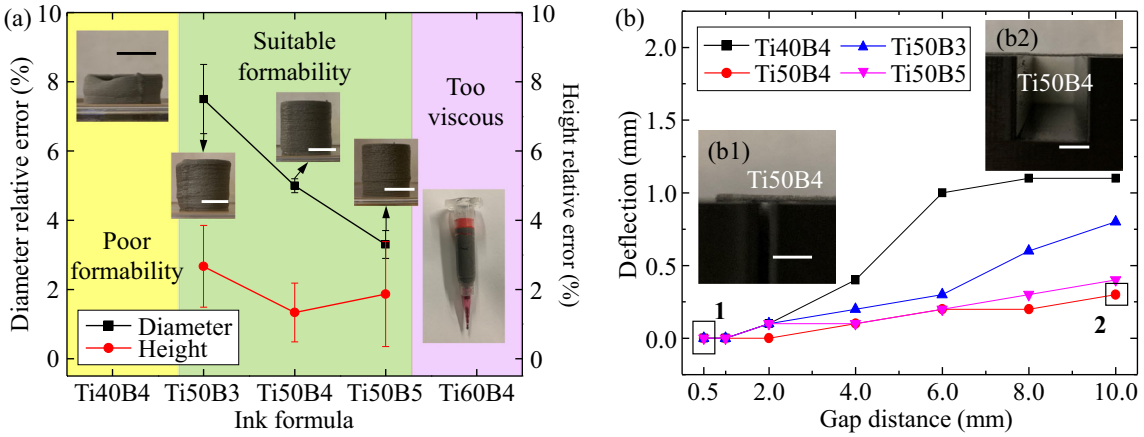

Fig. 3 **a** Relative errors of the diameter and height of the tubes printed using different Ti64 inks. Scale bars: 10.0 mm. **b** Deflections of the filament beams at different gap distances. Scale bars: 5.0 mm

shown in Fig. 3b. It was found that, at smaller gap distances (e.g., 0.5 and 1.0 mm), the beam deflections were negligible. The deflection increased with the increasing gap distance in the range of 2.0 to 10.0 mm. In addition, higher concentrations of Ti64 reduced the beam deflection greatly when the gap distance was relatively high. For example, the filament beam with 50% (v/v) Ti64 and 4% (w/v) bentonite had the deflection of around 0.25 mm at the gap distance of 10.0 mm, much lower than the deflection of the filament beam (~1.2 mm) with 40% (v/v) Ti64 and 4% (w/v) bentonite. This phenomenon can be attributed to the high yield stress of the Ti64 ink with a higher Ti64 concentration, as shown in Fig. 2c and Table 1. For self-supporting inks, the yield stress indicates the threshold energy for disrupting the inherent microstructure, which directly determines the mechanical stiffness of the printed structure [28, 31]. The ratio of deflection (δ_{max}) to beam span (L) can be used to assess the formability of a simply supported beam. For the ink with 50% (v/v) Ti64 and 4% (w/v) bentonite, $\delta_{max}/L = 0.12$ at the gap distance of 10.0 mm, which is lower than the reported ratios of filament beams from self-supporting inks [36], validating the good formability of the ink in this study. As a result, by comprehensively assessing the extrudability and formability in terms of vertical tube dimensional change and filament beam deflection, the Ti64 ink with 50% (v/v) Ti64 and 4% (w/v) bentonite was selected as the build material for printing complex 3D structures and acetabular cups.

Effects of printing conditions on filament formation and shape fidelity

After determining the optimal formula of Ti64 ink, the effects of printing conditions on filament size/morphology and shape fidelity were systematically investigated. First, filaments were printed on a substrate using different dispensing pressures, and the filament width and morphology were measured and imaged, as shown in Fig. 4a. It was found that, when the dispensing pressure was relatively low, the Ti64 ink could not form a continuous filament on the substrate. Instead, only segments were generated by the movement of the dispensing nozzle (see inset in Fig. 4a at the pressure of 0.1 bar). When the dispensing pressure was increased to 0.2 bar, a continuous filament could be deposited but its morphology was wave-shaped, therefore unsuitable for printing 3D structures with high accuracy. Meanwhile, when the dispensing pressure was increased to 0.3 bar and above, continuous filaments with well-defined morphology were printed. In addition, the filament width increased significantly from 0.8 to 2.1 mm in this pressure range.

Next, the effects of path speed on filament width were studied by varying the path speed from 5 to 9 mm/s in increments of 1 mm/s. As seen in Fig. 4b, the filament width decreased greatly from 1.23 to 0.5 mm. This is because the volume flow rate (Q) of the extruded Ti64 ink is constant when the dispensing pressure and nozzle geometries are unchanged. Filament width (D) is a function of path speed (v_p), as described by the equation $Q = \frac{1}{4}\pi D^2 v_p$ [30]. Thus, the filament width decreases with the path speed increasing.

Standoff distance is another important operating condition affecting the filament geometries and the shape fidelity of the printed pattern. Herein, the width and height of filaments using different standoff distances were measured, as shown in Fig. 4c. It was found that, when the standoff distance increased from 0.25 to 0.75 mm, the filament width decreased while the height increased. When the standoff distance varied in the range of 0.75–1.25 mm, neither filament width nor filament height presented obvious changes, and the filament width was close to the height. The reason is that,

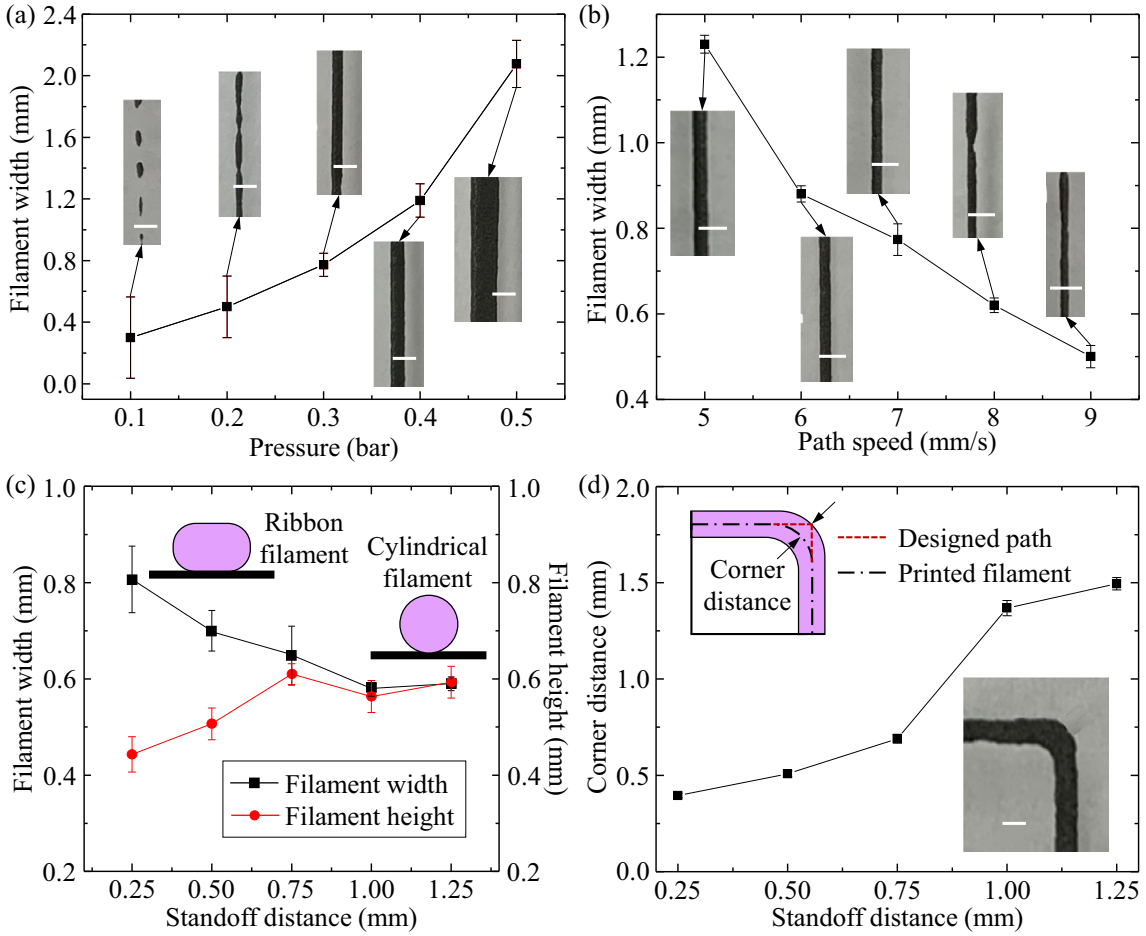

Fig. 4 Effects of printing conditions on filament formation and shape fidelity: filament width as a function of dispensing pressure (**a**) and path speed (**b**), the effects of standoff distance on filament width and height (**c**), and the shape fidelity of rectangular filament pattern (**d**). Scale bars: 2.0 mm. 1 bar=100 kPa

when the standoff distance is smaller than the filament diameter (~0.60 mm in this work), the nozzle tip compresses the filament during extrusion, resulting in the formation of ribbon filament with the width larger than the filament diameter and the height smaller than the diameter (inset of Fig. 4c) [37]. However, when the standoff distance exceeds the filament diameter, the nozzle compression effect disappears. Due to the high yield stress of ink material, the extruded filament can maintain the cylindrical shape when landing on the substrate, making the filament width equivalent to the filament height (inset of Fig. 4c).

The effects of standoff distance on the shape fidelity of printed filament pattern were characterized by a self-defined indicator, called corner distance, which was the distance between the designed path and printed filament at the corner of a rectangular filament pattern, as shown in the schematic in Fig. 4d. It was found that, at standoff distances lower than the filament diameter (i.e., 0.25 and 0.50 mm), the corner distances were relatively small (~0.5 mm). However, when the standoff distance increased from 0.75 to 1.25 mm, the corner distance increased greatly from ~0.6 to 1.5 mm. This is because when the standoff distance (d) is higher than the filament height (H), there is a gap (Δ) between the nozzle tip and the deposited filament, $\Delta=d-H$, which further results in a deposition delay time $\Delta t=\Delta/v_{\text{ink}}$, where v_{ink} represents the velocity of extruded Ti64 ink at the nozzle exit. As a result, the filament cannot be deposited exactly along the designed printing path (marked by the red dashed line in the schematic in Fig. 4d), which leads to the under-deposition phenomenon, especially at the deposition corners [38]. After evaluating the filament geometries and shape fidelity, the value of 0.75 was selected as the standoff distance to print complex 3D structures and acetabular cups in this work.

Maximum inclined angle of printable structure

Printing overhanging structures is one of the main persistent challenges in direct ink writing. In order to print an acetabular cup without creating supporting structures, the deposited

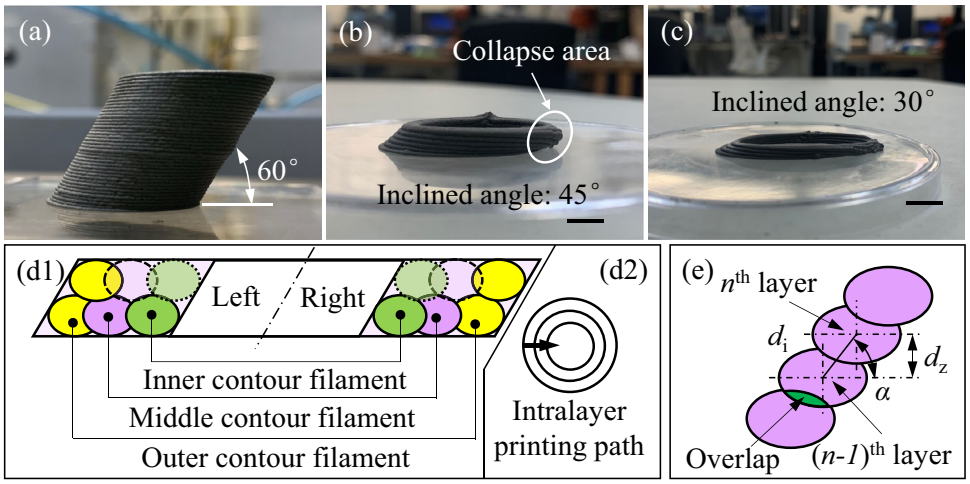

Fig. 5 Printed tubes with inclined angles of 60° (**a**), 45° (**b**), and 30° (**c**). **d1** Schematic of intralayer filament printing and **d2** intralayer printing path. **e** Schematic of printing each layer in an inclined tube. Scale bars: 5.0 mm

filaments and layers must be capable of self-supporting to a certain degree of overhang. Herein, the inclined tubes with different angles (60°, 45°, and 30°) were printed to explore the limitation of overhanging structures, as shown in Figs. 5a, 5b, and 5c, respectively. As seen from these figures, only the tube with the inclined angle of 60° was successfully printed with the height close to the designed value of 20 mm. When the height was above a given value, the tubes with the inclined angles of 30° and 45° collapsed during printing.

For printing an overhanging structure, the maximum inclined angle is essentially determined by the overlap-induced intralayer and interlayer filament fusions, which are, respectively, affected by the selection of printing paths along the horizontal and vertical directions. Herein, each layer of an inclined tube is composed of three concentrically printed filaments: outer contour filament, middle contour filament, and inner contour filament, as shown in Fig. 5d1. The intralayer (horizontal) printing path is from the outer to the inner contours (Fig. 5d2). Thus, when printing a new layer, the left section of the outer contour filament is deposited first, which overlaps with and is fully supported by the outer and middle contour filaments in the previous layer. In contrast, when the dispensing nozzle is continuously moved to print the rest of the outer contour filament, the resultant right section only overlaps with the outer contour filament in the previous layer, forming an overhanging structure, which is easy to collapse, as illustrated in Fig. 5d1. The inner contour filament is the last to be deposited. Its left section overlaps with both the middle contour filament in the current layer and the inner contour filament in the previous layer, while the right section overlaps with three filaments: both the inner and middle contour filaments in the previous layer, and the middle contour filament in the current layer, as shown in Fig. 5d1. This horizontal printing path intrinsically constrains that the inclined tubes cannot maintain good shapes at their outer overhanging surfaces, as marked in Fig. 5b. In this scenario, decreasing the vertical step distance may be a potential solution, which can effectively increase the overlap area at the overhanging section, especially when the inclined angle is relatively large.

The tube collapse in this work is also attributed to the unsuitable printing path control along the vertical direction. As shown in the schematic in Fig. 5e, when printing a 3D structure, the most common technique to design the vertical printing path is to select a constant step distance (d_z) regardless of the inclined angle (α). However, the interlayer mechanical properties of the 3D structure mainly depend on the overlap-induced interlayer fusion, which can be quantified by the interlayer distance $d_i = d_z/\sin\alpha$. When the inclined angle changes from 90° to 60°, 45°, and 30°, the interlayer distance increases from d_z to $1.2d_z$, $1.4d_z$, and finally to $2.0d_z$, resulting in a decrease in the overlap area. Thus, the poor interlayer fusion leads to the collapse of the printed structure, even though the self-supporting capability of each layer is excellent. As a result, for overhanging structure printing, the best strategy to design a vertical path is to control a constant interlayer distance by dynamically adjusting the vertical step distance. Since the 3D printer used in this work lacks the ability to customize the vertical printing path, 60° was selected as a threshold value for the direct ink writing of acetabular cups. The constant vertical step distance was used to print the cup structure concentrically only when the inclined angle was less than or equal to 60°. Above 60°, straight filaments were deposited based on the parallel trajectory to form each layer.

Curing depth analysis

Curing depth must be considered when creating parts from photo-curable materials, because part geometries, especially thickness, may be constrained. To determine the maximum curing depth of the proposed Ti64 ink, the samples were exposed under UV radiation for different time periods. The

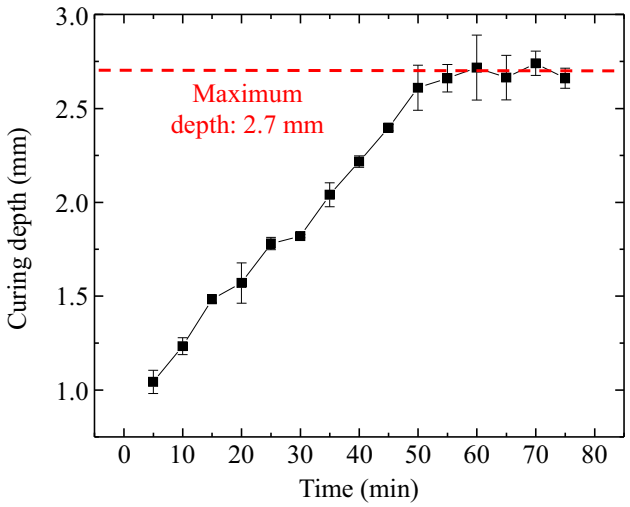

Fig. 6 Curing depth as a function of exposure time

unidirectional curing depth was measured as shown in Fig. 6. It was found that, when the exposure time increased from 5 to 50 min, the curing depth increased from 1.0 to 2.6 mm. However, further increasing the exposure time (from 55 to 75 min) did not significantly change the unidirectional curing depth.

The theoretical curing depth of UV crosslinkable materials with a solid particle phase can be qualitatively analyzed using the following equation [39]:

$$C_{\mathrm{d}} = \frac{2d}{3\varphi\beta(\Delta n)^2}\ln\left(\frac{E_{\mathrm{c}}}{E_{\max}}\right),$$

where C_{d} denotes the curing depth, d denotes the particle size, φ denotes the volume fraction of the solid phase, β is a parameter that relates to the wavelength of radiation as well as interparticle spacing, Δn denotes the difference between the refractive index of the UV curable material and the solid particles, E_{c} denotes the critical energy dosage required to crosslink the material, and $E_{\max}$ is the maximum energy applied to the material. In this study, the large volume of Ti64 particles in the ink material results in the sharp attenuation of maximum energy that can reach the interior of the samples. When the interior maximum energy is equivalent to E_{c}, the curing depth cannot be increased anymore regardless of the exposure time. Thus, based on the measurement, the maximum unidirectional curing depth was around 2.7 mm, which indicates that, theoretically, a cup structure with up to 5.4 mm wall thickness can be fully cured, which approximates to the wall thickness of commercial acetabular cups [40]. The exposure time of 60 min was used for curing printed acetabular cups.

Complex 3D structure printing

Complex 3D structures, including lattices with three different gap distances and a honeycomb (see Figs. 7a1–7a3), were printed to demonstrate the printing capability of the proposed method. When the gap distance was 3 mm, the filament deflection was almost negligible. However, when the gap distance increased to 5 mm, some filaments presented observable deflections. The printed honeycomb is illustrated in Fig. 7b. Each cell exhibited a well-defined shape with uniform wall thickness. In addition, since there was no overhanging section, the entire honeycomb was printed by using a constant vertical step distance. By carefully selecting the printing conditions, the surface morphology of the honeycomb was relatively good, and no pronounced layered surface was observed.

Fabrication of acetabular cups

In order to fabricate an acetabular cup, a hemispherical cup structure was first printed at room temperature via direct ink writing, as shown in Movie S1 (Supplementary Information). The intralayer printing path, as illustrated in the inset of Fig. 8a, prevented the potential collapse at the outer overhanging surface. Subsequently, UV radiation was applied to crosslink PEGDA in the cup structure. The cup after curing is shown in Fig. 8a. The cup was designed to have a diameter of 40 mm, height of 20 mm, and thickness of 5 mm. After crosslinking, these key dimensions were measured as 40.97 mm, 23.44 mm, and 5.18 mm (as summarized in Table 2). The relative errors of thickness and diameter were 3.60% and 2.43%, respectively, indicating the high printing accuracy along the horizontal directions. The relatively large variation in height (relative error of 17.20%) is attributed to the over-deposition phenomenon when printing each layer along the vertical direction. In this work, a lower vertical step distance was selected to ensure the adhesion between adjacent layers in the overhanging section of the cup structure, which resulted in vertically over-deposited Ti64 ink, thus making the height exceed the designed value. Designing the dynamic vertical step distances may be a potential solution, in which d_{i} is kept constant to simultaneously fulfill the requirements of sufficient self-supporting capability and high dimensional accuracy along the vertical direction.

Next, multi-step heat treatment was applied to the cup structure, as shown in Fig. 8b. The first step aimed to decompose crosslinked PEGDA, which had a decomposition temperature of 175–400 °C. Thus, the furnace temperature was increased to 500 °C to achieve this task efficiently [41]. The temperature was much lower than the melting temperature of Ti64. As a result, this step theoretically did not affect the formation of microstructure within the cup. Because the decomposition products mainly included carbon

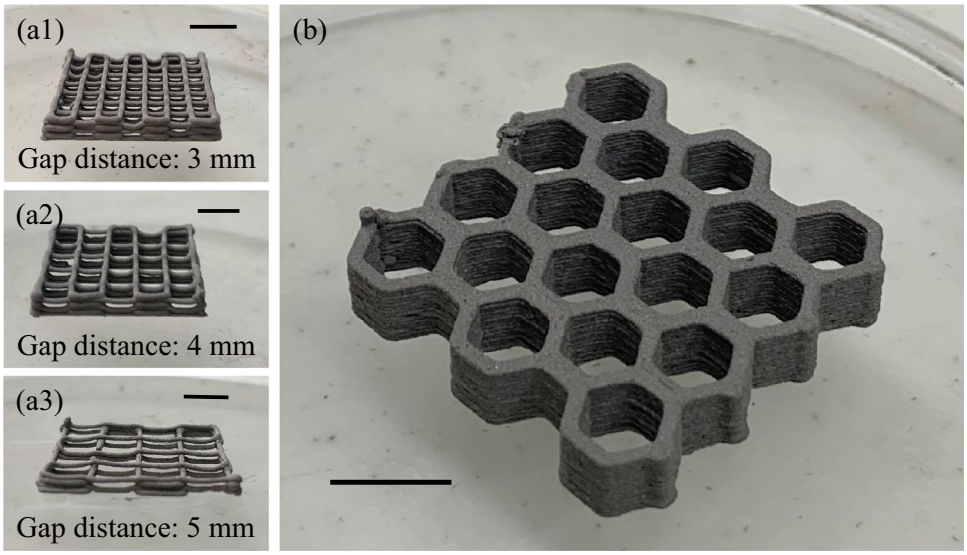

Fig. 7 **a** Lattice structures with gap distances of 3 mm (**a1**), 4 mm (**a2**), and 5 mm (**a3**). **b** Honeycomb with well-defined shape. Scale bars: 5.0 mm

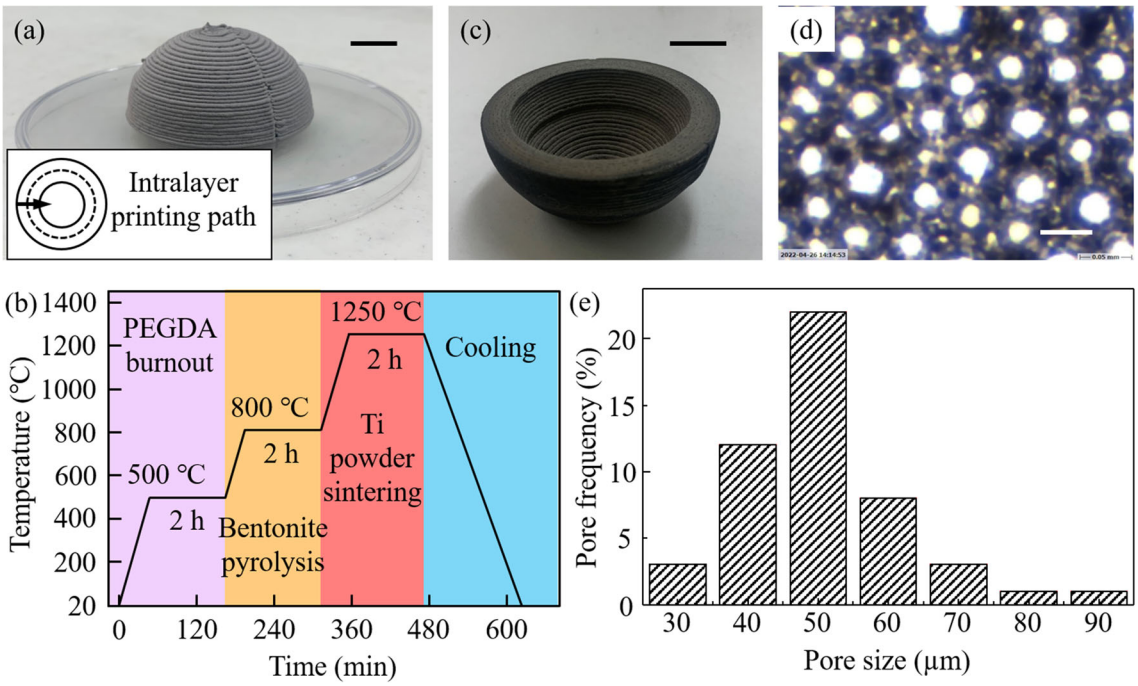

Fig. 8 **a** Cup structure printed at room temperature via direct ink writing (inset: intralayer printing path). **b** Multi-step heat treatment procedure. **c** Acetabular cup after heat treatment. **d** Image of porous microstructure. **e** Micropore size distribution and frequency. Scale bars: 10 mm in (**a**) and (**c**), and 50 μm in (**d**)

Table 2 Key dimensions of the acetabular cup

	Designed value (mm)	After curing (mm)	Relative error (%)	After heat treatment (mm)	Relative error (%)	Relative error (before and after heat treatment) (%)
Height	20	23.44	17.20	23.63	18.20	0.80
Thickness	5	5.18	3.60	5.12	2.40	1.20
Diameter	40	40.97	2.43	40.89	2.23	0.20

monoxide, carbon, methyl radical, ethylenyl, carbon dioxide, acetaldehyde, and water [42], a vacuum furnace was used to effectively remove all these products during heat treatment to prevent the undesired oxidation and carbonization of Ti64 particles. In the second step, the furnace temperature was increased to 800 °C, as the decomposition temperature of bentonite fell in the range of 575–800 °C. At this temperature, bentonite particles pyrolyze into alkanes, alkenes and tertiary amines, and carbon dioxide [43], which were rapidly removed from the furnace. Herein, the time duration of this step was selected as 2 h [43] to ensure the full decomposition of PEGDA and bentonite particles, resulting in the formation of micropores within the cup structure. Meanwhile, at 800 °C, Ti64 particles were sintered gradually based on the mechanism of solid phase sintering [44] to maintain the shape integrity of the cup structure. In the third step, the furnace temperature was increased to 1250 °C [45] to further sinter Ti64 particles together and enhance the mechanical properties. In the last step, the furnace temperature was gradually reduced to room temperature.

The cup structure after heat treatment is illustrated in Fig. 8c. The key dimensions were measured as follows: height of 23.63 mm, thickness of 5.12 mm, and diameter of 40.89 mm. The relative errors (Re_X) of these key dimensions before and after heat treatment were calculated as 0.80%, 1.20%, and 0.20%, respectively (as summarized in Table 2), via the equation $\mathrm{Re}_X = \frac{|X_C - X_H|}{X_C} \times 100\%$, where X_C and X_H represent the measured dimensions after curing and after multi-step heat treatment, respectively; $X =$ height, thickness, or diameter. Since the cup dimensions after heat treatment were very close to the ones before heat treatment, it is concluded that the designed multi-step heat treatment can efficiently remove PEGDA and bentonite to form microscale porous structure without causing pronounced geometric shrinkage to the macroscale cup structure. The porous microstructure of the acetabular cup was imaged as shown in Fig. 8d. The microscale pore was uniformly distributed in the acetabular cup. The pore size distribution is summarized in Fig. 8e. It is found that more than 20% of the pores had the average size of around 50 μm, close to the size of bentonite particle used in this work; approximately 12.5% and 7.5% of the pores had an average size of 40 and 60 μm, respectively. In total, 40% of pores were sized in the range of 40–60 μm, indicating that relatively uniform porous structure was generated within the acetabular cup with controllable pore sizes. It is noted that the average pore size in this work was smaller than that of available acetabular cups (ranging from 150 to 600 μm [46]). Because bentonite particle size is adjustable in a wide range, in the future, larger bentonite particles will be used to further test the feasibility of controlling the pore size using the proposed heat treatment. In addition, Ti64 particle size may affect the porosity and pore size. As reported in the literature [47], when it is below 150 μm, the sintering time needs to be carefully controlled, because a longer sintering process may result in the decreased porosity of the final products.

Conclusions and future work

This study presents a direct ink writing method to print cup structures at room temperature, which have been sintered using a multi-step heat treatment process to create porous acetabular cups. Because of the excellent self-supporting capability of the Ti64 ink, some complex 3D structures, such as inclined tube, lattice, and honeycomb, have been successfully printed to validate the broad fabrication space of the proposed direct ink writing method. In addition, the ink formula, printing conditions, structural limitation, and maximum curing depth have been systematically studied. It is found that the rheological properties are more sensitive to the Ti64 concentration change and less sensitive to the variation in bentonite concentration. Simply supported filament beams could be printed and the beam deflection could be enhanced by either reducing the gap distance or increasing the Ti64 concentration. For the printing conditions, the increases in dispensing pressure and path speed result in the increase and decrease in filament width, respectively. The standoff distance significantly affects the filament morphology as well as the shape fidelity of printed patterns. In addition, an unsuitable printing path control along the vertical direction may lead to the collapse of overhanging structures, even though the self-supporting capability of each layer is excellent. Moreover, the large volume of Ti64 particles in the ink material attenuates the maximum UV energy that can reach the interior of the printed structures, leading to limited maximum curing depth. Finally, the designed heat treatment procedure can effectively decompose PEGDA and bentonite in the printed structures, leading to the formation of micropores with relatively uniform pore size distribution.

Since the main purpose of this study was to demonstrate the feasibility of the proposed direct ink writing approach for printing acetabular cups at room temperature, the mechanical stiffness of the cups was not measured. In the future, the key mechanical properties (e.g., elastic modulus, wear resistance, and fracture strength) as well as microstructures of acetabular cups after printing, UV crosslinking and each step of heat treatment will be comprehensively characterized. The effects of pore size and porosity on the mechanical properties will also be studied. In addition, bentonite additive with larger particle sizes will be used to prepare Ti64 inks, and the relationship between bentonite particle size and pore size/distribution within sintered acetabular cups will be further investigated.

Supplementary Information The online version contains supplementary material available at https://doi.org/10.1007/s42242-022-00222-2.

Acknowledgements This research was supported by the Micro Grant (PG20473) at the University of Nevada, Reno, USA.

Author contributions NV, WH, and AKK performed the experiments, collected the data, and conducted the data analysis and interpretation. NV, WH, and YJ wrote the manuscript. YJ generated the concept and designed the study. LR and PLM involved in writing, critical editing, and proofreading the manuscript.

Declarations

Conflict of interest The authors declare that they have no conflict of interest.

Ethical approval This article does not contain any studies with human or animal subjects performed by any of the authors.

References

1. Jaber SA, Affatato S (2018) An overview of in vitro mechanical and structural characterization of hip prosthesis components. In: Zivic F, Affatato S, Trajanovic M, et al. (Eds.), Biomaterials in Clinical Practice. Springer Cham, Switzerland, pp 585–599. https://doi.org/10.1007/978-3-319-68025-5_22
2. Bozic KJ, Kurtz SM, Lau E et al (2009) The epidemiology of revision total hip arthroplasty in the United States. J Bone Joint Surg 91(1):128–133. https://doi.org/10.2106/JBJS.H.00155
3. Patel A, Pavlou G, Mújica-Mota RE et al (2015) The epidemiology of revision total knee and hip arthroplasty in England and Wales: a comparative analysis with projections for the United States. A study using the national joint registry dataset. Bone Joint J 97(8):1076–1081. https://doi.org/10.1302/0301-620X.97B8.35170
4. Singh JA, Yu S, Chen L et al (2019) Rates of total joint replacement in the United States: future projections to 2020–2040 using the national inpatient sample. J Rheumatol 46(9):1134–1140. https://doi.org/10.3899/jrheum.170990
5. Dall'Ava L, Hothi H, Henckel J et al (2021) Osseointegration of retrieved 3D-printed, off-the-shelf acetabular implants. Bone Joint Res 10(7):388–400. https://doi.org/10.1302/2046-3758.107.BJR-2020-0462.R1
6. Kienapfel H, Sprey C, Wilke A et al (1999) Implant fixation by bone ingrowth. J Arthroplasty 14(3):355–368. https://doi.org/10.1016/S0883-5403(99)90063-3
7. Hu CY, Yoon TR (2018) Recent updates for biomaterials used in total hip arthroplasty. Biomater Res 22(1):33. https://doi.org/10.1186/s40824-018-0144-8
8. McTighe T, Brazil D, Keppler L et al (2015) Metallic modular taper junctions in total hip arthroplasty. Reconstr Rev 5(2):29–42. https://doi.org/10.15438/rr.5.2.108
9. Velásquez-García LF, Kornbluth Y (2021) Biomedical applications of metal 3D printing. Annu Rev Biomed Eng 23(1):307–338. https://doi.org/10.1146/annurev-bioeng-082020-032402
10. Menon V, Aranas C Jr, Saha G (2022) Cold spray additive manufacturing of copper-based materials: review and future directions. Mater Sci Add Manuf 1(2):1–20. https://doi.org/10.18063/msam.v1i2.12
11. Miyagawa T, Matsumoto K, Komura S et al (2021) Mid-term results of total hip arthroplasty using a three-dimensional porous titanium acetabular cup: an examination of micromotion using subject-specific finite element analysis. BMC Musculoskelet Disord 22(1):1–8. https://doi.org/10.21203/rs.3.rs-155777/v1
12. Nadagouda MN, Ginn M, Rastogi V (2020) A review of 3D printing techniques for environmental applications. Curr Opin Chem Eng 28:173–178. https://doi.org/10.1016/j.coche.2020.08.002
13. Seifi M, Salem A, Beuth J et al (2016) Overview of materials qualification needs for metal additive manufacturing. JOM 68(3):747–764. https://doi.org/10.1007/s11837-015-1810-0
14. Vaithilingam J, Prina E, Goodridge RD et al (2016) Surface chemistry of Ti6Al4V components fabricated using selective laser melting for biomedical applications. Mater Sci Eng C 67:294–303. https://doi.org/10.1016/j.msec.2016.05.054
15. Sing SL, An J, Yeong WY et al (2016) Laser and electron-beam powder-bed additive manufacturing of metallic implants: a review on processes, materials and designs. J Orthop Res 34(3):369–385. https://doi.org/10.1002/jor.23075
16. Heinl P, Rottmair A, Körner C et al (2007) Cellular titanium by selective electron beam melting. Adv Eng Mater 9(5):360–364. https://doi.org/10.1002/adem.200700025
17. Heinl P, Müller L, Körner C et al (2008) Cellular Ti–6Al–4V structures with interconnected macro porosity for bone implants fabricated by selective electron beam melting. Acta Biomater 4(5):1536–1544. https://doi.org/10.1016/j.actbio.2008.03.013
18. Parthasarathy J, Starly B, Raman S et al (2010) Mechanical evaluation of porous titanium (Ti6Al4V) structures with electron beam melting (EBM). J Mech Behav Biomed Mater 3(3):249–259. https://doi.org/10.1016/j.jmbbm.2009.10.006
19. Murr LE, Gaytan SM, Martinez E et al (2012) Next generation orthopaedic implants by additive manufacturing using electron beam melting. Int J Biomater 2012:245727. https://doi.org/10.1155/2012/245727
20. Sing SL (2022) Perspectives on additive manufacturing enabled beta-titanium alloys for biomedical applications. Int J Bioprint 8(1):478. https://doi.org/10.18063/ijb.v8i1.478
21. Maszybrocka J, Skrabalak G, Karolus M et al (2017) Morphology and surface topography of Ti6Al4V lattice structure fabricated by selective laser sintering. Bull Pol Acad Sci 65(1):85–92. https://doi.org/10.1515/bpasts-2017-0011
22. Suwanpreecha C, Manonukul A (2022) A review on material extrusion additive manufacturing of metal and how it compares with metal injection moulding. Metals 12(3):429. https://doi.org/10.3390/met12030429
23. Mohammadizadeh M, Lu H, Fidan I et al (2020) Mechanical and thermal analyses of metal-PLA components fabricated by metal material extrusion. Inventions 5(3):44. https://doi.org/10.3390/inventions5030044
24. Elsayed H, Rebesan P, Giacomello G et al (2019) Direct ink writing of porous titanium (Ti6Al4V) lattice structures. Mater Sci Eng C 103:109794. https://doi.org/10.1016/j.msec.2019.109794
25. Xu C, Liu T, Guo W et al (2020) 3D printing of powder-based inks into functional hierarchical porous TiO_2 materials. Adv Eng Mater 22(3):1901088. https://doi.org/10.1002/adem.201901088
26. Pack RC, Compton BG (2020) Material extrusion additive manufacturing of metal powder-based inks enabled by carrageenan rheology modifier. Adv Eng Mater 62(3):2000880. https://doi.org/10.1002/adem.202000880
27. Peng S, Mooraj S, Feng R et al (2021) Additive manufacturing of three-dimensional (3D)-architected CoCrFeNiMn high-entropy alloy with great energy absorption. Scr Mater 190:46–51. https://doi.org/10.1016/j.scriptamat.2020.08.028
28. Jin Y, Liu C, Chai W et al (2017) Self-supporting nanoclay as internal scaffold material for direct printing of soft hydrogel composite structures in air. ACS Appl Mater Interfaces 9(20):17456–17465. https://doi.org/10.1021/acsami.7b03613
29. Jin Y, Compaan A, Chai W et al (2017) Functional nanoclay suspension for printing-then-solidification of liquid materials.

ACS Appl Mater Interfaces 9(23):20057–20066. https://doi.org/10.1021/acsami.7b02398
30. Jin Y, Chai W, Huang Y (2017) Printability study of hydrogel solution extrusion in nanoclay yield-stress bath during printing-then-gelation biofabrication. Mater Sci Eng C 80:313–325. https://doi.org/10.1016/j.msec.2017.05.144
31. Jin Y, Shen Y, Yin J et al (2018) Nanoclay-based self-supporting responsive nanocomposite hydrogels for printing applications. ACS Appl Mater Interfaces 10(12):10461–10470. https://doi.org/10.1021/acsami.8b00806
32. Kalakkunnath S, Kalika DS, Lin H et al (2006) Viscoelastic characteristics of UV polymerized poly(ethylene glycol) diacrylate networks with varying extents of crosslinking. J Polym Sci B Polym Phys 44(15):2058–2070. https://doi.org/10.1002/polb.20873
33. Ma T, Lv L, Ouyang C et al (2021) Rheological behavior and particle alignment of cellulose nanocrystal and its composite hydrogels during 3D printing. Carbohydr Polym 253:117217. https://doi.org/10.1016/j.carbpol.2020.117217
34. Prud'homme RK, Wu G, Schneider DK (1996) Structure and rheology studies of poly(oxyethylene-oxypropylene-oxyethylene) aqueous solution. Langmuir 2(20):4651–4659. https://doi.org/10.1021/la951506b
35. Jiang J, Burger C, Li C et al (2007) Shear-induced layered structure of polymeric micelles by SANS. Macromolecules 40(11):4016–4022. https://doi.org/10.1021/ma062654j
36. Sakhakarmy M, Tian S, Raymond L et al (2021) Printability study of self-supporting graphene oxide-laponite nanocomposites for 3D printing applications. Int J Adv Manuf Technol 114(1):343–355. https://doi.org/10.1007/s00170-021-06870-5
37. Athanasiadis M, Pak A, Afanasenkau D et al (2019) Direct writing of elastic fibers with optical, electrical, and microfluidic functionality. Adv Mater Technol 4(7):1800659. https://doi.org/10.1002/admt.201800659
38. Jin Y, Zhao D, Huang Y (2018) Study of extrudability and standoff distance effect during nanoclay-enabled direct printing. Bio-des Manuf 1(2):123–134. https://doi.org/10.1007/s42242-018-0009-y
39. Allen Brady G, Halloran JW (1997) Stereolithography of ceramic suspensions. Rapid Prototyp J 3(2):61–65. https://doi.org/10.1108/13552549710176680
40. Meding JB, Small SR, Jones ME et al (2013) Acetabular cup design influences deformational response in total hip arthroplasty. Clin Orthop Relat Res 471(2):403–409. https://doi.org/10.1007/s11999-012-2553-7
41. Zhang Y, Yin MJ, Ouyang X et al (2020) 3D μ-printing of polytetrafluoroethylene microstructures: a route to superhydrophobic surfaces and devices. Appl Mater Today 19:100580. https://doi.org/10.1016/j.apmt.2020.100580
42. Ozaydin-Ince G, Gleason KK (2009) Thermal stability of acrylic/methacrylic sacrificial copolymers fabricated by initiated chemical vapor deposition. J Electrochem Soc 157(1):D41. https://doi.org/10.1149/1.3251308
43. Ramos Filho FG, Mélo TJA, Rabello MS et al (2005) Thermal stability of nanocomposites based on polypropylene and bentonite. Polym Degrad Stab 89(3):383–392. https://doi.org/10.1016/j.polymdegradstab.2004.12.011
44. Olmos L, Cabezas-Villa JL, Bouvard D et al (2020) Synthesis and characterisation of Ti6Al4V/xTa alloy processed by solid state sintering. Powder Metall 63(1):64–74. https://doi.org/10.1080/00325899.2020.1719689
45. Dewidar MM, Lim JK (2008) Properties of solid core and porous surface Ti-6Al-4V implants manufactured by powder metallurgy. J Alloys Compd 454(1–2):442–446. https://doi.org/10.1016/j.jallcom.2006.12.143
46. Li JP, de Wijn JR, Van Blitterswijk CA et al (2006) Porous Ti_6Al_4V scaffold directly fabricating by rapid prototyping: preparation and in vitro experiment. Biomaterials 27(8):1223–1235. https://doi.org/10.1016/j.biomaterials.2005.08.033
47. Azeez AA, Danyuo Y, Obayemi JD (2020) Effect of particle size and sintering time on the mechanical properties of porous Ti–6Al–4V implant. SN Appl Sci 2(5):819. https://doi.org/10.1007/s42452-020-2637-z